Technical University of Denmark

DTU

# Probing the crossover in CO desorption from single crystal to nanoparticulate Ru model catalysts

Murphy, Shane; Strebel, Christian Ejersbo; Vendelbo, Søren Bastholm; Conradsen, Christian Nagstrup; Tison, Yann; Nielsen, Kenneth; Bech, Lone; Nielsen, Rasmus Munksgård; Johansson, Martin; Chorkendorff, Ib; Nielsen, Jane Hvolbæk

[Link back to DTU Orbit](Link back to DTU Orbit)

**DTU Library**
Technical Information Center of Denmark

**PAPER**

# Probing the crossover in CO desorption from single crystal to nanoparticulate Ru model catalysts

S. Murphy, C. Strebel, S. B. Vendelbo, C. Conradsen, Y. Tison, K. Nielsen, L. Bech, R. M. Nielsen, M. Johansson, I. Chorkendorff and J. H. Nielsen*

Using model catalysts, we demonstrate that CO desorption from Ru surfaces can be switched from that typical of single crystal surfaces to one more characteristic of supported nanoparticles. First, the CO desorption behaviour from Ru nanoparticles supported on highly oriented pyrolytic graphite was studied. Both mass-selected and thermally evaporated nanoparticles were deposited. TPD spectra from the mass-selected nanoparticles exhibit a desorption peak located around 410 K with a broad shoulder extending from around 480 K to 600 K, while spectra obtained from thermally evaporated nanoparticles exhibit a single broad feature from $\sim$350 K to $\sim$450 K. A room temperature deposited 50 Å thick Ru film displays a characteristic nanoparticle-like spectrum with a broad desorption feature at $\sim$420 K and a shoulder extending from $\sim$450 K to $\sim$600 K. Subsequent annealing of this film at 900 K produced a polycrystalline morphology of flat Ru(001) terraces separated by monatomic steps. The CO desorption spectrum from this surface resembles that obtained on single crystal Ru(001) with two large desorption features located at 390 K and 450 K due to molecular desorption from terrace sites, and a much smaller peak at $\sim$530 K due to desorption of dissociatively adsorbed CO at step sites. In a second experiment, ion sputtering was used to create surface defects on a Ru(0 1 54) single crystal surface. A gradual shift away from the desorption spectrum typical of a Ru(001) surface towards one resembling desorption from supported Ru nanoparticles was observed with increasing sputter time.

## I. Introduction

While surface science studies of macroscopic single crystal surfaces have yielded much valuable insight into the fundamental principles of heterogeneous catalysts, the well-known materials gap between surface science and industrial catalysis exists.[1–4] Typically, industrial catalysts are much more complex in nature than the single crystal surfaces encountered in many surface science studies. A better representation of these materials can be obtained by studying an ensemble of nanoparticles supported on a well-defined planar substrate.[5–7] Such model systems can be used to investigate the effect of the particle size and the influence of the support material on reactivity. Moreover, nanoparticulate model catalysts are more suited to studying the correlation between structure and activity in structure-sensitive reactions because of the resemblance to industrial catalysts, which comprise a high density of various active sites such as edge or corner sites, as compared to single crystal

surfaces where the number of equivalent step or kink sites can be outweighed by several orders of magnitude by less-active terrace sites.[8,9] As part of our efforts to understand the materials gap we have been investigating the crossover in desorption behaviour between the two model catalyst systems, *i.e.* single crystal surfaces *versus* supported nanoparticles. Here we present details of our investigation of the thermal desorption of CO from a Ru(0 1 54) single crystal surface and from Ru nanoparticles supported on highly oriented pyrolytic graphite (HOPG).

Ruthenium is a versatile catalyst, which has been particularly investigated with respect to methanation and Fischer–Tropsch synthesis.[10–12] As an elementary step in this process the adsorption of CO on single crystal Ru(001) has been studied extensively by various surface science methods.[13–22] CO adsorbs on the Ru(001) basal surface in an upright position *via* the carbon atom at all coverages up to saturation at around 2/3 of a monolayer.[23–25] The CO molecules adsorb in on-top positions up to a coverage of 1/3 of a monolayer, forming a $(\sqrt{3}\times\sqrt{3})R30°$ adlayer structure.[26–28] At higher coverages, the $(\sqrt{3}\times\sqrt{3})R30°$ structure is disrupted as strong repulsive interactions cause CO molecules to be displaced from on-top positions (though the exact microstructure of the higher coverage overlayers is still debated[29]).

*Center for Individual Nanoparticle Functionality,*
*Department of Physics, Technical University of Denmark,*
*2800 Kgs. Lyngby, Denmark. E-mail: jane@fysik.dtu.dk;*
*Fax: + 45 4593 2399*

The change in adlayer structure is reflected in the CO desorption behaviour. For coverages up to 1/3 of a monolayer CO desorbs in a single peak decreasing from 480 K to 450 K with increasing coverage ($\alpha_1$ peak), while for higher coverages a second peak develops around 350–400 K ($\alpha_2$ peak).[18,22,30,31] In addition to these peaks, which are due to desorption of molecularly adsorbed CO, an additional much smaller peak may also be observed at around 530 K, arising from the desorption of CO that has been dissociatively adsorbed at step sites ($\beta$ peak).[13,19,21,22,32] This was demonstrated by Shincho et al.,[13] Yamada et al.[19] and Zubkov et al.[21,22] using isotopic scrambling experiments, which rely on the recombination and desorption of atomic carbon and oxygen originating from the dissociative adsorption of CO. It was furthermore demonstrated that deposition of carbon at surface steps blocked them for dissociative adsorption of CO and resulted in the disappearance of the $\beta$ peak from CO desorption spectra.[22,32]

The CO desorption from more open Ru single crystal surfaces has also been investigated and displays similarities to TPD spectra obtained from the Ru(001) plane.[33–37] For the Ru(110) plane, for example, the $\alpha_1$ and $\alpha_2$ peaks at similar temperatures were observed along with two $\beta$ peaks attributed to dissociation of CO at different sites. The desorption of $CO_2$ from the Ru(110) surface at 380–450 K was furthermore observed.

If we consider the information available with regard to CO desorption from supported Ru nanoparticles, a number of studies have investigated CO desorption from Ru catalysts prepared by chemical impregnation of $SiO_2$ and $Al_2O_3$ supports.[38–42] Typically, two main features were observed in these studies, a low temperature feature located between 350 K and 475 K, and a higher temperature feature located between 600 K and 700 K.[38–42] The two features at lower temperatures agree well with the double-peak spectrum obtained from Ru(001)[18,22,30,31] and the variation in the temperatures recorded for the desorption features in the different studies could be attributed to the different heating rates used. Moreover, where desorption experiments were performed in reactors under a He carrier gas flow,[38–41] the measured desorption temperatures could also be influenced by readsorption of CO, which was found to shift desorption peaks to higher temperatures.[39] The desorption of $CO_2$ was also observed in some of these studies, which could be taken as evidence of CO dissociation occuring over the Ru nanoparticles.[39,40,42]

Here, we demonstrate that it is possible to link the desorption behaviour of supported nanoparticles (both mass-selected particles formed in a magnetron-sputter gas-aggregation source and vapour-deposited particles) and that of the single crystal surface using two approaches. In the first case, we demonstrate the transition from nanoparticle-like CO desorption behaviour to single-crystal surface behaviour in Ru nanoparticles supported on HOPG. In the second case, we demonstrate the reverse transition from single-crystal surface to nanoparticle-like CO desorption behaviour by means of $Ar^+$ ion pre-sputtering of the Ru(0 1 54) surface.

## II. Experimental

The experiments were performed in three separate UHV systems. The experiments on Ru nanoparticles were performed in a multichamber ultrahigh vacuum (UHV) system (Omicron, Multiscan Lab) with a base pressure in the low $10^{-11}$ mbar region.[43,44] This system is equipped with facilities for combined scanning tunneling microscopy (STM) and scanning electron microscopy (SEM), as well as Auger electron spectrsocopy (AES), ion scattering spectroscopy (ISS) and temperature programmed desorption (TPD) measurements. The thermal desorption experiments on the Ru(0 1 54) surface were performed in a UHV chamber with a base pressure below $10^{-10}$ mbar, which is equipped with facilities for TPD and AES, as well as a high-pressure cell.[32] STM measurements on the Ru(0 1 54) surface were performed in a UHV chamber with a base pressure below $10^{-10}$ mbar,[45] which is equipped with X-ray photo-electron spectroscopy (XPS) and an Aarhus-type STM.[46]

### A  Ru nanoparticles on HOPG

The HOPG substrates (SPI-1, 7 mm × 7 mm × 0.5 mm) were cleaved in air and mounted in sample holders incorporating a pyrolytic boron nitride (PBN) radiative heater, which is capable of heating the sample to temperatures in excess of 975 K. A C-type thermocouple (W-5 at.% Re/W-26 at.% Re) was placed in contact with the substrate in order to monitor and control the sample temperature via a PID controller (Eurotherm 2408). Upon insertion into UHV, the samples were outgassed for several hours at 775 K to outgas adsorbed contaminants prior to use. Two different methods were used to deposit Ru nanoparticles.

In the first method, mass-selected nanoparticles were deposited from an inert-gas aggregation source (Mantis Deposition Ltd.), which is described in detail elsewhere.[43,44] Briefly, a flux of Ru atoms is produced by a magnetron sputter head, which is condensed into nanoparticles upon contact with cooled Ar gas atoms. The ionised fraction of the nanoparticle beam is filtered to select the mass of the nanoparticles to be deposited using a quadrupole mass filter, before the nanoparticles are soft-landed (i.e. they have a kinetic energy of $\leq 0.1$ eV atom$^{-1}$) onto HOPG substrates. For these studies, we have investigated both as-cleaved HOPG and surfaces that have been sputtered for 15 min with 500 eV $Ar^+$ ions at a current density of $\sim 1$ $\mu$A cm$^{-2}$ and subsequently outgassed at 935 K. The 15 min sputtering causes defects in at least the first two layers of the surface.[47]

In the second method, Ru films were deposited on HOPG by electron-beam evaporation of a 99.99% purity Ru rod. The substrates were either as-cleaved or sputtered for 30 s with 500 eV $Ar^+$ ions under the same conditions as those given above. Sputtering for only 30 s produces approximately 5% of defects in the topmost surface layer. The substrate was grounded while the Ru rod was held at a positive bias of 500 V.[48] A quartz crystal balance was used to monitor the deposition rate (typically 0.46–0.9 Å min$^{-1}$) and estimate the final film thickness.

Ion Scattering Spectroscopy (ISS) was used to confirm the cleanliness of the HOPG substrate and the deposited Ru nanoparticles and thin films. The ISS spectra were recorded using 1 keV $He^+$ ions produced by a differentially pumped electron impact ion source (ISE 100, Omicron Nanotechnology). The reflected ions were detected at a 147° scattering angle with a hemispherical energy analyser.

10334 | Phys. Chem. Chem. Phys., 2011, **13**, 10333–10341

This journal is © the Owner Societies 2011

TPD experiments were performed in the preparation chamber of the UHV system. The samples were dosed with a 1 : 1 mixture of two different isotopically labeled CO molecules, namely $^{13}C^{16}O$ (CIL, 99% $^{13}C$, <10% $^{18}O$)[49] and $^{12}C^{18}O$ (CIL, 2% $^{16}O$). Both gases were dosed simultaneously using separate leak valves until a total chamber pressure of $2 \times 10^{-8}$ mbar was attained. The ratio of the two gases was held constant by monitoring the mass spectrometer signal for each component. The samples were dosed in this manner for 10 min, corresponding to an exposure of nine Langmuir, which was sufficient to saturate the surface. It was possible to observe the saturation in the CO uptake during dosing with the mass spectrometer. The sample temperature was then ramped at a rate of 1 K s$^{-1}$ in UHV and the CO desorption from the substrate was analysed using a differentially pumped Balzers QMA 125 quadrupole mass spectrometer. The spectrometer was equipped with an oxygen-free high conductivity (OFHC) copper sniffer tip with a 1 mm diameter aperture, which is positioned within 0.5 mm of the sample surface. This arrangement allows the local gas composition above the sample surface to be measured with negligible contribution from the sample holder or surroundings.

The isotope exchange reaction ($^{12}C^{18}O + ^{13}C^{16}O \rightarrow ^{12}C^{18}O + ^{13}C^{16}O + ^{13}C^{18}O + ^{12}C^{16}O$) allows us to determine the relative amount of CO that has been dissociated on the surface from the TPD spectra. If the adsorbed $^{13}C^{16}O$ and $^{12}C^{18}O$ molecules dissociate on the surface, the dissociated species can scramble and recombine into the four possible CO isotopologues $^{12}C^{16}O$, $^{13}C^{16}O$, $^{12}C^{18}O$ and $^{13}C^{18}O$. The TPD mass spectrometer signals of 28 amu, 29 amu, 30 amu and 31 amu were background subtracted and integrated to find the total desorption of each isotopologue. Particular attention was paid to the $^{13}C^{18}O$ signal as this does not have a high natural background in the UHV chamber like $^{12}C^{16}O$, and does not contribute to molecular desorption like either $^{13}C^{16}O$ or $^{12}C^{18}O$. Assuming an equal probability for scrambling into each of the four products, the amount of desorbed $^{13}C^{18}O$ will account for approximately one quarter of the total amount of adsorbed CO molecules that have been dissociated.

STM was performed at room temperature in constant current mode, using electrochemically etched W tips without any in-vacuum treatments other than applying a series of voltage pulses (typically 4–9 V for 10–100 ms) or scanning for several lines with increased bias ($U \approx 2$ V) in order to condition the tip. The typical tunnel parameters used to image the particles in this study were $U = 10$–600 mV for the gap bias and $I = 0.1$–0.8 nA for the tunnel current. Slow scan speeds were adopted with a typical line scan frequency of about 0.5–1 Hz.

## B Ru(0 1 54) surface

The samples used for these experiments are Ru(0 1 54) single crystals (Mateck GmbH.), which on average expose 27-atom wide (001) terraces separated by monatomic steps. Due to the hexagonal close-packed structure of Ru, the steps will be of two alternating structures, one with three-fold symmetry and the other with four-fold symmetry.[22] For the TPD experiments presented here, a Ru(0 1 54) sample was cleaned by repeated

cycles of sputtering with 1 keV Ar$^+$ ions at 800 K for 30 min, oxidation in $10^{-7}$ mbar O$_2$ at 1100 K for 10 min, reduction in $10^{-6}$ mbar H$_2$ at 500 K for 30 min, and finally annealing to 1200 K in UHV for 1 min. The cleanliness of the sample was checked by AES and CO TPD and oxygen titration measurements (which were used to check for carbon contamination).[32] TPD measurements were performed using a (Balzers 125) quadrupole mass spectrometer fitted with a differentially pumped OFHC copper sniffer tip with a 2 mm diameter circular aperture. This orifice was positioned at a distance of 0.5 mm from the sample surface, so that only desorption from the front side of the single crystal was measured. The sample temperature was measured by means of a C-type thermocouple spot-welded to the side of the crystal. The crystal was mounted on tungsten filaments which were used to provide direct current heating. During TPD measurements the sample temperature was ramped linearly at a rate of 2 K s$^{-1}$. The sample was mounted in the UHV chamber out of direct line-of-sight of the ionisation gauge in order to avoid hot-filament induced chemistry.

A second Ru(0 1 54) sample was used for the STM measurements, which was cleaned using a similar procedure to that described above.[50] The sample was sputtered using 1 keV Ar$^+$ ions by quickly rastering a 3 mm diameter ion beam with a current density of 18 μA cm$^{-2}$ across the sample surface. The cleanliness was checked using STM, XPS and CO TPD measurements (the TPD setup was similar to the one described above). STM measurements were performed at room temperature in constant current mode, using electrochemically etched W tips. Images were typically recorded with a gap bias of 1 V and a tunneling current of 0.4–1 nA.

## III. Results

### A Ru nanoparticles on HOPG

The morphology of the mass-selected nanoparticles has been described in detail elsewhere.[43,44] Depositions were carried out so that between 10% and 40% of the HOPG surface was covered by a monodisperse distribution of nanoparticles with a mean diameter in the range from 2 nm to 15 nm.[51] Transmission electron microscopy (TEM) was used to measure the particle size distributions obtained after mass filtering and it was found that the diameters of the nanoparticles were distributed within ±15% of the mean diameter. TEM measurements revealed that smaller nanoparticles displayed more well-defined facets, while larger nanoparticles were found to be irregular in shape with evidence of significant surface roughness.[44] An example of a STM image of mass-selected 9.7 nm Ru nanoparticles on HOPG is shown in Fig. 1(a). We have previously established that the morphology of nanoparticles supported on sputtered or as-cleaved HOPG is basically the same.[43] Fig. 1(b) shows the total CO desorption spectrum obtained from 9.7 nm Ru nanoparticles. The TPD spectrum is characterised by a desorption peak located around 410 K, followed by a broad shoulder extending from around 480 K to 600 K. The molecularly- and dissociatively-adsorbed components of the TPD spectrum [also shown in Fig. 1(b)] can be deconvoluted by utilising the isotope exchange reaction,
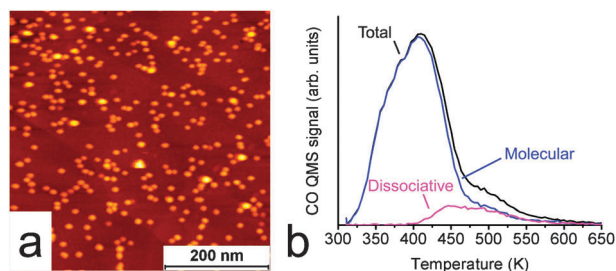
This journal is © the Owner Societies 2011

*Phys. Chem. Chem. Phys.*, 2011, **13**, 10333–10341 | 10335

**Fig. 1** STM and CO desorption from size-selected Ru nanoparticles on HOPG. (a) STM image of 9.7 nm Ru nanoparticles on sputtered HOPG. (b) CO TPD spectrum obtained from 9.7 nm Ru nanoparticles on as-cleaved HOPG, showing the total CO desorption, as well as the contributions from molecularly- and dissociatively-adsorbed CO.
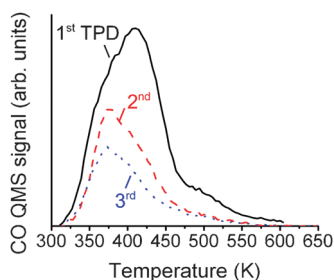


**Fig. 2** Three successive CO TPD spectra obtained from 9.7 nm mass-selected Ru nanoparticles on as-cleaved HOPG, showing a drop in the desorption area.

$^{12}C^{18}O + {}^{13}C^{16}O \rightarrow {}^{12}C^{18}O + {}^{13}C^{16}O + {}^{13}C^{18}O + {}^{12}C^{16}O$, which is expected to occur after CO dissociation. It is clear that the large desorption peak located around 410 K corresponds to the molecularly desorbed component (*i.e.* mass-29 and mass-30 CO), while desorption of dissociatively adsorbed CO (here only mass-31 CO is used in the analysis), which displays peaks at 450 K and 530 K, is largely responsible for the broad shoulder up to 600 K seen in the total CO desorption spectrum.

Fig. 2 shows three successive CO TPD spectra obtained from 9.7 nm Ru nanoparticles on as-cleaved HOPG. The main desorption feature, which is located around 410 K in the first TPD, shifts to 375 K in the second and third spectra. There is also a substantial loss in the CO desorption area (63%) between the first and second TPD, and a smaller drop (30%) between the second and third TPD. This behavior was consistently observed for different nanoparticle sizes on as-cleaved and sputtered HOPG. It was usually found that the loss in desorption area became small or negligible after the second or third TPD. Three mechanisms can be identified as candidates for this deactivation: (1) sintering, (2) poisoning by loose carbon from the support, and (3) annealing-out of the initial surface roughness of the as-deposited nanoparticles. We have previously confirmed by STM that small nanoparticles (*e.g.* ~3 nm) deposited onto as-cleaved HOPG do sinter at elevated temperatures (775–975 K).[43] We have also performed oxygen titration experiments (not presented here), which indicate that carbon is present at the surface of the nanoparticles after heating to temperatures comparable to those encountered during the desorption experiments. We can therefore confirm that both of these mechanisms contribute to the deactivation of the
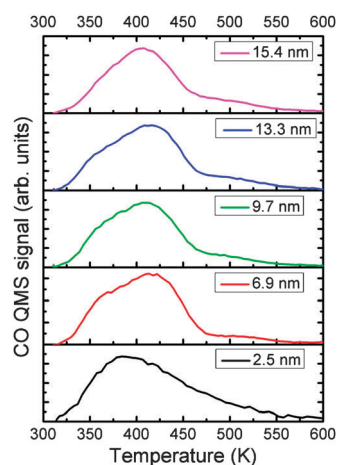


**Fig. 3** CO TPD spectra obtained for different sized Ru nanoparticles supported on as-cleaved HOPG. The curves have been normalised to the same peak height.

nanoparticles, while the third proposed mechanism requires further investigation by performing annealing experiments in the TEM.

Fig. 3 compares the total CO TPD spectra obtained from nanoparticles of different sizes supported on as-cleaved HOPG. The curves have been normalised to the same peak height in order to compare their shape. The TPD spectra are qualitatively similar being characterised by a broad desorption feature with a peak around 410–420 K and a broad shoulder extending from ~450 K to ~600 K. The low-temperature shoulder along with the high-temperature tail seems to increase as the nanoparticle size decreases, being most prominent for the 2.5 nm size. In previous studies of PVD grown Ru nanoparticles on mica, the position of the CO desorption feature was not observed to change substantially with the mean particle size.[52]

In addition to investigating the CO desorption behavior from mass-selected nanoparticles produced using the inert-gas aggregation source, we have also investigated the CO desorption behavior of PVD-grown Ru nanoparticles on HOPG. The morphology of these nanoparticles has been discussed in detail elsewhere.[43] Briefly, Ru films deposited onto as-cleaved HOPG at room temperature were found to display bimodal growth with small round nanoparticles decorating the substrate step edges and large flat nanoparticles formed on the terraces. The mean diameter of these nanoparticles was between 3 nm and 5.5 nm and their mean height was around 1.5 nm, while the spread in the measured size distributions was of the order of ±30%. On sputtered HOPG, room temperature deposition of Ru results in the formation of small round nanoparticles with a narrow size distribution. In this case, the mean particle diameter was approximately 2.3 nm and the mean height was close to 1.3 nm, while the spread in the measured particle size was ±20%. Examples of these two nanoparticle morphologies are shown in Fig. 4(a) and (c), which show STM images of 1 Å Ru films deposited on as-cleaved and sputtered HOPG, respectively. These images were obtained after CO TPD measurements were made. The average diameter of the nanoparticles from the 1 Å deposition was 5.2 ± 2.1 nm on the terraces
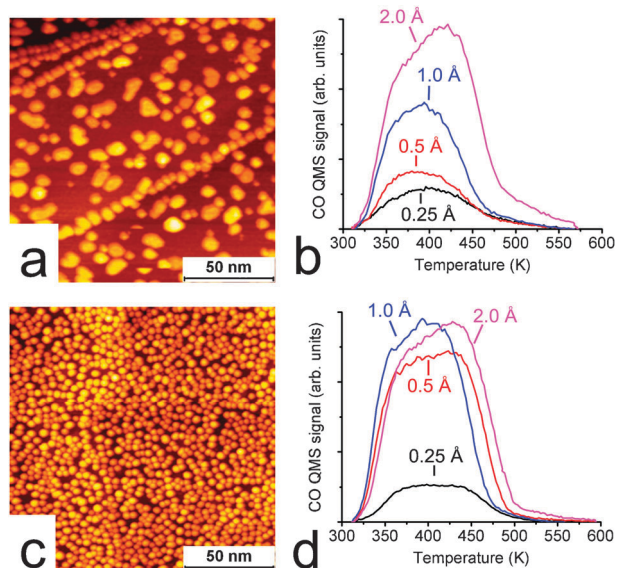
Fig. 4 STM and CO TPD measurements of Ru films deposited onto HOPG. (a) STM image of a 1 Å Ru film deposited onto as-cleaved HOPG. The average diameter of the terrace nanoparticles was 5.2 nm and their average height was 1.7 nm. (b) CO TPD spectra from 0.25–2.0 Å Ru films on as-cleaved HOPG. (c) STM image of a 1 Å Ru film deposited onto HOPG that has been pre-sputtered with 500 eV Ar$^+$ ions for 30 s. The average nanoparticle diameter was 2.1 nm and the average height was 1.1 nm. (d) CO TPD spectra from 0.25–2.0 Å Ru films on sputtered HOPG.
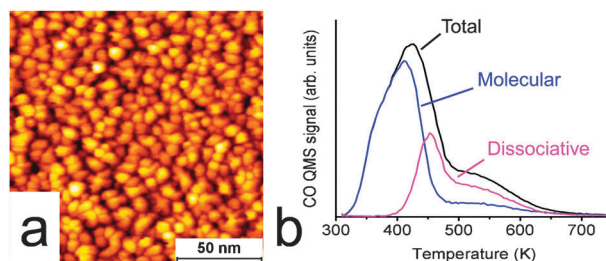


Fig. 5 (a) STM image of a 50 Å Ru film deposited on as-cleaved HOPG at room temperature. (b) The corresponding CO TPD spectrum obtained from the film, showing the total CO desorption, as well as the contributions from molecularly- and dissociatively-adsorbed CO.
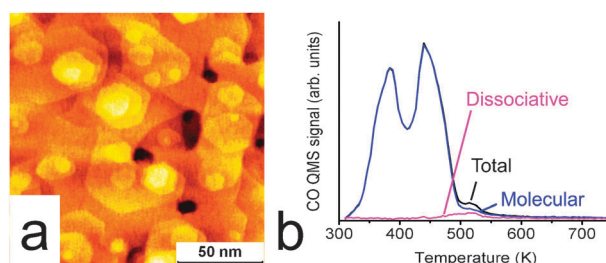


Fig. 6 (a) STM image of a 50 Å Ru film deposited on as-cleaved HOPG after annealing in UHV at 900 K for 10 min. (b) The corresponding CO TPD spectrum obtained from the film, showing the total CO desorption, as well as the contributions from molecularly- and dissociatively-adsorbed CO.

and 3.9 ± 1.0 nm along the steps, in the case of deposition on the as-cleaved HOPG surface [cf. Fig. 4(a)], and 2.1 ± 0.5 nm in the case of deposition on the pre-sputtered HOPG [cf. Fig. 4(c)]. The heights of the nanoparticles were on the order of 1–2 nm.[43] Fig. 4(b) and (d) show CO desorption spectra for different nominal film thicknesses deposited on (b) as-cleaved HOPG and (d) HOPG sputtered for 30 s with 500 eV Ar$^+$ ions. The desorption spectra are characterised by a single broad feature from ~350 K to ~450 K. For Ru nanoparticles deposited on as-cleaved HOPG the CO desorption area increases continuously with increasing nominal film thickness in the thickness range investigated here [see Fig. 4(b)]. This reflects the fact that the HOPG surface is gradually covered by Ru nanoparticles with increasing film thickness. By contrast, there is a substantial jump in the CO desorption area from the 0.25 Å to 0.5 Å Ru films on sputtered HOPG, after which the amount of CO desorbing from the surface remains approximately constant. In this case, the HOPG surface is partially exposed for the 0.25 Å film, but is almost completely saturated by Ru nanoparticles at a nominal film thickness of 0.5 Å [see Fig. 4(d)]. Thereafter, the total Ru surface area exposed to CO remains approximately constant for thicker films.[43] As was the case for the mass-selected nanoparticles, successive TPD spectra of the vapour-deposited nanoparticles (not shown here) also displayed deactivation of the nanoparticles between the first and second TPD measurements.

We have examined the CO desorption behaviour of these PVD-grown Ru films up to the extreme case of a 50 Å Ru thin film. Fig. 5(a) shows an image of a 50 Å Ru film deposited on as-cleaved HOPG at room temperature. The surface morphology

of the film comprises nanoparticles with a mean diameter of 6 ± 2 nm. The substrate cannot be imaged by STM as the film is several layers thick. Fig. 5(b) shows the corresponding CO desorption spectrum, which shows a single broad desorption feature centered around 420 K and a broad shoulder from 500 K to 600 K. After obtaining this spectrum the film was annealed for 10 min at 900 K in UHV. The resulting film morphology, shown in Fig. 6(a), is polycrystalline with large flat terraces separated by monatomic steps. The corresponding CO desorption spectrum is shown in Fig. 6(b), and shows two desorption features at ~390 K and ~450 K. An additional, smaller peak can be seen at ~530 K. This spectrum agrees well with the typical desorption spectrum obtained from the Ru(001) facet.[18,22,30–32] The two principal peaks can be attributed to desorption of molecularly adsorbed CO from the terraces (α peaks), while the smaller peak can be attributed to desorption of dissociatively adsorbed CO from step sites (β peak).[13,22]

## B Ru (0 1 54) surface

Fig. 7(a) and (b) show STM images of the non-sputtered Ru (0 1 54) surface and the same surface after sputtering for 5 min, respectively. The non-sputtered surface is characterised by terraces with a width varying between 4 nm and 10 nm, encompassing the expected average terrace width of 6.5 nm (corresponding to 27 atoms), and separated by straight monatomic steps with a measured height of 0.21 ± 0.01 nm, which is in good agreement with the distance between the (001) planes of ruthenium. In comparison, the steps on the sputtered surface display a high degree of roughness, while small islands are
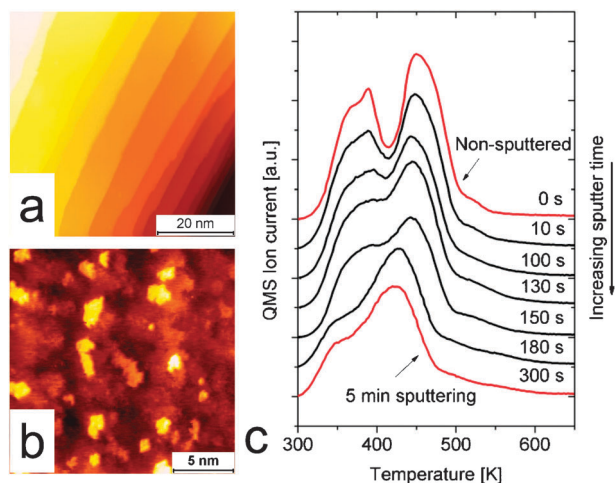
**Fig. 7** STM and CO TPD measurements from a Ru(0 1 54) single crystal surface before and after Ar$^+$ ion sputtering. (a) STM image of the clean non-sputtered Ru(0 1 54) surface. (b) STM image of the same surface after sputtering with 1 keV Ar$^+$ ions for 5 min. (c) Sequence of CO TPD spectra obtained from the Ru(0 1 54) surface after sputtering with 1 keV Ar$^+$ ions for increasing periods of time.

evident on the terraces, which are presumably formed by surface restructuring as a result of the sputtering process.

Fig. 7(c) shows a sequence of CO desorption spectra obtained from the Ru(0 1 54) surface after different periods of sputtering with 1 keV Ar$^+$ ions at room temperature. The CO desorption spectrum from the non-sputtered surface shows two desorption peaks located at 390 K and 460 K that are characteristic of CO desorption from (001) terraces ($\alpha_1$- and $\alpha_2$-peaks) and a peak at ~535 K corresponding to the dissociative adsorption at step sites ($\beta$-peak).[18,22,30–32] However, with increased surface sputtering a gradual transition is observed between the double-peak spectrum towards a single broad feature centered around 420 K. The desorption feature seen at 390 K on the non-sputtered surface gradually disappears with increased sputtering time until it is no more than a shoulder on the low-temperature side of the main desorption feature seen for the 5 min sputtered surface. In addition, the peak at 460 K on the non-sputtered surface gradually shifts down in temperature with increased sputtering time until the feature is located around 420 K.

It should be pointed out once again that the STM and TPD data of the Ru(0 1 54) surface presented here were obtained in two different UHV systems. However, in both cases the cleanliness of the surface before and after sputtering was confirmed (by XPS in the case of the STM measurements, and by AES and oxygen titration measurements in the case of the TPD experiments) to ensure that a contamination level below ~1% was obtained. Moreover, CO TPD measurements were also performed in the STM system, which yielded qualitatively similar results to those presented here.

## IV. Discussion

### A Comparison of desorption energies

As demonstrated in Section IIIA the isotope exchange reaction unambiguously identifies molecular desorption being responsible

for the main desorption feature at 410–420 K, while dissociative adsorption is responsible for smaller features at 430 K and 500 K. For comparison, Table 1 gives a summary of the CO desorption features reported from various studies (including this study) of supported Ru nanoparticles and single crystal surfaces. For the purposes of comparing our results to literature values, desorption energies based on the data presented in Table 1 are calculated and presented together in Fig. 8. The desorption features were classified into two categories corresponding to molecular (first-order) and dissociative (second-order) adsorption on the basis of the literature surveyed in Section I. The first-order desorption energies were calculated using the Redhead equation[53] and assuming a pre-exponential factor of $10^{13}$ s$^{-1}$. The second-order desorption energies were solved iteratively using the equation:[54]

$$E_{des}(\theta) = RT_p \ln\left(\frac{2\theta\nu(\theta)RT_p^2}{E_{des}(\theta)\beta}\right) \qquad (1)$$

where $T_p$ is the desorption peak temperature, $\theta$ is the remaining CO coverage (assumed to be half the initial coverage) and $R$ is the gas constant. The desorption energy $E_{des}$ and the pre-exponential factor $\nu$ are both assumed to be constant with coverage, where $\nu = 10^{13}$ s$^{-1}$.

From our CO TPD experiments on graphite-supported nanoparticles, we calculate desorption energies of 112–113 kJ mol$^{-1}$, which agree reasonably well with the values calculated from previous studies of oxide-supported nanoparticles,[38–42] particularly

**Table 1** Summary of CO desorption features from saturation coverages of CO on various supported Ru nanoparticles and single crystal surfaces. The peak temperatures for the different desorption features and the heating rate are listed. Temperature intervals for some features have been indicated by hyphenated values. The desorption features have been classified into two categories; $T_\alpha$ representing molecular desorption and $T_\beta$ representing dissociative adsorption

| System | $T_\alpha$/K | $T_\beta$/K | Heating rate/K s$^{-1}$ |
|---|---|---|---|
| Ru NPs/HOPG[a] | 410-420 | 450, 530 | 1 |
| 50 Å Ru/HOPG (as-deposited)[a] | 420 | 450, 530 | 1 |
| 50 Å Ru/HOPG (annealed)[a] | 390, 450 | 530 | 1 |
| Ru/mica[52] | ~410 | | 1.5 |
| Ru/Al$_2$O$_3$[38] | 375 | 475, 600–630 | 1 |
| Ru/Al$_2$O$_3$[39] | 460 | 620 | 1 |
| Ru/SiO$_2$[40] | 450 | 650 | 1.5 |
| Ru/SiO$_2$[41] | 405, 473 | 698 | 0.17 |
| (001)[18,30] | 405-420, 465-480 | | 5 |
| (109)[22] | 400, 450 | 535 | 2 |
| (0 1 54)[32] | ~390, ~460 | 535 | 2 |
| (0 1 54) non-sputtered[a] | ~390, ~460 | 535 | 2 |
| (0 1 54) sputtered[a] | ~420 | | 2 |
| Ru(S)-[15(001)×2(100)][20] | 400, 470 | 520 | 9 |
| (1 1 10)[13] | 460 | ~580 | 15 |
| (2 $\bar{1}$ 10)[19] | ~460 | ~530 | 7.7 |
| (2 $\bar{1}$ 22)[19] | ~470 | ~530 | 5.2 |
| (101)[33] | ~480 | ~520 | 30 |
| (100)[34] | ~403, ~495 | | 8 |
| (100)[35] | 350, 380, 500 | | 4 |
| (100)[36] | 375, ~400, ~500 | | 8.7 |
| (110)[37] | 400, 440-460 | 500, 540 | 3 |

[a] This work.
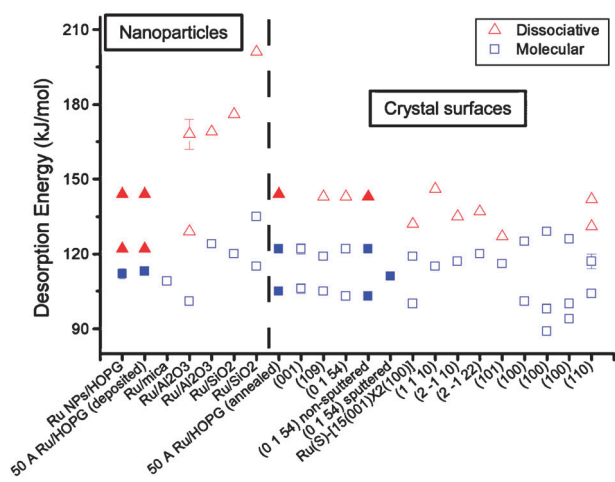
**Fig. 8** Summary of the desorption energies calculated using the data presented in Table 1. Open symbols are data taken from previous studies, while filled symbols are taken from the present study. Temperature intervals for certain features are indicated by error bars.

with the case of PVD-grown nanoparticles on mica, see Fig. 8.[52] On the other hand, the desorption energies for dissociatively adsorbed CO (122 kJ mol$^{-1}$ and 144 kJ mol$^{-1}$) calculated for our graphite supported nanoparticles are much lower than those estimated from the data available from these other studies, where a high temperature desorption feature was typically observed between 600 K and 700 K, corresponding to desorption energies around 164–201 kJ mol$^{-1}$. The origins of these high temperature peaks were investigated by McCarty and Wise[38] who used isotopic scrambling of $^{13}C^{16}O$ and $^{12}C^{18}O$ to investigate the dissociation of CO over Ru/Al$_2$O$_3$. While they observed isotope exchange at ~475 K (129 kJ mol$^{-1}$), which is in reasonable agreement with the results obtained in the present study, they also observed an unusual behaviour at ~600 K where the levels of $^{18}O$ containing isotopologues ($^{12}C^{18}O$ and $^{13}C^{18}O$) were found to decrease, while the levels of $^{16}O$ containing isotopologues ($^{12}C^{16}O$ and $^{13}C^{16}O$) increased. This indicated that an excess of $^{16}O$ was being derived from some source, though the Al$_2$O$_3$ support was ruled out as a potential source on the basis of blank TPD measurements. As a result, the nature of the higher temperature desorption feature observed between 600 K and 700 K in most of these studies has not been adequately explained and may be linked to the method of preparing the catalyst, *i.e.* wet impregnation.

## B  Origins of the nanoparticle desorption spectra

Compared to the single crystal surfaces, the desorption energies calculated for both molecularly- and dissociatively-adsorbed CO on the supported nanoparticles in the present study generally fall within the range of energies calculated for both the basal Ru surface and for more open surfaces. This may be attributed to the fact that the nanoparticles expose facets with different orientations. In the simplest representation of the nanoparticle shape, *i.e.* the Wulff construction, the nanoparticles will principally comprise (001), (101) and (100) facets, as these have the lowest surface free energy.[44,55] Consequently, the desorption spectra should mainly contain

contributions from these facets. However, we have previously shown that the shape of the mass-selected Ru nanoparticles departs from the Wulff construction,[44] and consequently the CO desorption behaviour is expected to be more complex than one based on this simple model. In addition to the orientation of the facets exposed on the nanoparticle surface, their size may also influence the desorption spectra. For example, it has been shown that the double-peak molecular desorption feature characteristic of the Ru(001) facet appears to be inhibited on stepped Ru single crystal surfaces when the average terrace width is sufficiently narrow.[13,19] Shincho *et al.*[13] found a single desorption feature during CO desorption from a Ru(S)-[5(001)×(110)] surface comprising five-atom wide (001) terraces,[56] whereas Westre *et al.*[20] and Zubkov *et al.*[22] observed two desorption features during desorption from saturated CO coverages on Ru(S)-[15(001)×2(100)] and Ru(S)-[9(001)×2(101)] surfaces comprising fifteen- and nine-atom wide (001) terraces, respectively. There are two possible explanations for this: (1) the terraces are too small to accommodate the ordered overlayer structures found on extended (001) facets and (2) a localised lattice strain is produced in the vicinity of steps, which has been shown to influence CO adsorption.[57] In the case of nanoparticles, where facet sizes can be comparably small to the terrace widths found on highly stepped single crystal surfaces, both of these mechanisms may play a role in determining the CO desorption behaviour from the nanoparticle surface. In Fig. 4, a change in the desorption spectrum may be present for the smallest (*i.e.* 2.5 nm) of the nanoparticles with an increase in the low-temperature shoulder and in the high-temperature tail. This suggests that different sites are relatively more abundant on the very small nanoparticles. Detailed investigations of several mass-selected nanoparticle sizes in the 1–5 nm range are needed before conclusions can be made, but it is interesting to note that carbon-supported cobalt nanoparticles, which—just like ruthenium—are catalysts for the Fischer–Tropsch (FT) reaction, show an increase in FT activity for the very small sizes.[58]

It should also be pointed out that pre-adsorption of a small amount of O$_2$ or H$_2$O onto the Ru(001) surface prior to CO adsorption can substantially shift the TPD spectrum from the double-peak spectrum to a spectrum similar to that obtained from supported nanoparticles.[59,60] However, in the present study ISS measurements performed on the nanoparticles both before and after the TPD experiments showed no evidence of oxygen (*i.e.* below the detection limit of 1% of a monolayer). This indicates that the shape of the TPD spectra is related to the structure of the clean nanoparticle surface. We therefore conclude that the TPD spectrum obtained from the nanoparticles can be linked to a combination of the compact facet size on the nanoparticle surface, and the fact that more open facets may be exposed. This is particularly true when the shape of the nanoparticles departs from the equilibrium shape. Moreover, we observe two features corresponding to desorption of dissociatively adsorbed CO at 450 K and 530 K (desorption energies of 122 kJ mol$^{-1}$ and 144 kJ mol$^{-1}$, respectively), which point to the presence of two main dissociation sites for CO on the nanoparticle surface.

This journal is © the Owner Societies 2011

*Phys. Chem. Chem. Phys.*, 2011, **13**, 10333–10341 | 10339

## C Crossover in desorption behaviour

A key result of the present study is that we have been able to demonstrate the crossover in CO desorption behaviour between Ru nanoparticles and the basal Ru surface simply by annealing a PVD-grown thin film to high temperature. The fact that we observe dissociative CO adsorption both before and after annealing the film proves that the surface remains free of carbon from the support, which would otherwise block the undercoordinated sites responsible for CO dissociation on the surface.[22,32] A key element in the formation of the polycrystalline film in Fig. 6 is that an epitaxial relationship exists between the vapour deposited Ru and the HOPG surface. In the case of the mass-selected nanoparticles discussed earlier, no such epitaxial relationship is obtained since the nanoparticles are formed before deposition and assume random orientations when landed on the surface. As expected, it was therefore not possible to obtain a morphology like that shown in Fig. 6(a) by annealing a thin film of mass-selected nanoparticles at 900 K. However, we believe that this should in principle be possible if higher anneal temperatures are used, which was not possible with the existing experimental set-up.

It was also possible to demonstrate the reverse transition in desorption behaviour between that of the basal Ru surface and that of Ru nanoparticles by sputtering a single crystal surface. As the amount of sputtering increases the amount and type of surface sites change as probed by the CO TPDs in Fig. 7(c). It is seen that the amount of step sites giving rise to the small shoulder at 510 K for the non-sputtered surface increases with more sputtering and changes into a broad feature ranging from below 500 K to at least 600 K for the most sputtered surface. This indicates that the sputtering introduces more undercoordinated sites, and that different kinds of sites exist giving rise to different desorption temperatures of dissociatively adsorbed C and O. More detailed STM studies of the sputtered surface would be required to identify the different site configurations.

It was found that the molecular desorption feature at 390 K gradually disappears, while the desorption feature at 460 K, corresponding to more strongly bound molecular CO, shifts downwards in temperature with increased sputtering. This can be rationalized as an effect of having smaller average terrace sizes on the sputtered surface. As mentioned earlier, the terraces may be too small to accommodate the ordered overlayer structures found on extended (001) facets. Also, it has previously been suggested by Jakob et al.[57] that the region 1–2 nm from the step exhibits a compressed lattice, which would result in a weaker binding of CO.[61] With a higher abundance of terrace sites in close proximity to a step, more weakly bonded CO would be expected, in excellent agreement with our CO TPDs.

It is observed that desorption of CO from the sputtered surface starts immediately upon heating from room temperature, whereas the desorption from the non-sputtered surface does not start until around ∼20 K above room temperature. This indicates that our CO TPD spectra from the sputtered surfaces do not probe all sites available on the surface, as the TPD spectrum from the non-sputtered surface appears to do. As such, one should not attempt to rationalise the apparent trend in Fig. 7(c) that the total CO desorption area decreases with increased sputtering time, until TPD experiments starting from below room temperature are performed.

## V. Summary

We have compared the CO desorption characteristics of a stepped Ru(001) single crystal with Ru nanoparticles supported on graphite and have established the crossover in CO desorption behaviour between the two. Our main findings were:

• Mass-selected Ru nanoparticles deposited on HOPG display a single CO desorption feature around 410–420 K followed by a broad shoulder from 480 K to 600 K. Utilising the isotope exchange reaction we have established that the larger peak at 410–420 K is principally due to molecularly desorbing CO, while the shoulder is due to desorption of dissociatively adsorbed CO.

• Successive TPD measurements result in deactivation of the nanoparticles due to sintering and/or poisoning of the catalyst surface by carbon from the support. A possible third deactivation mechanism involves annealing-out the non-equilibrium surface features of the nanoparticles.

• Ru nanoparticles grown on HOPG by vapour deposition display broadly the same characteristics as the mass-selected nanoparticles. Moreover, by annealing a PVD-grown thin film we demonstrate a crossover in CO desorption spectra from that characteristic of supported nanoparticles to one characteristic of a stepped Ru(001) single crystal surface.

• Starting from a stepped Ru(001) single crystal surface we have also demonstrated the reverse transition from single crystal to nanoparticle-like CO desorption behaviour by means of Ar$^+$ ion sputtering.

We have shown that it is possible to vary the desorption behaviour between the two model catalyst systems by using straightforward sample preparation methods. These results demonstrate the complementary nature of both model catalyst systems and affirm the validity of studying both in order to narrow the materials gap to more complex industrial catalysts. With further work, for example using more well-defined Wulff constructed nanoparticles or mesoscale crystals,[62] even greater insight into the crossover between the desorption behavior of single crystal surfaces and supported nanoparticles can be obtained.

## References

1 D. W. Goodman, *Chem. Rev.*, 1995, **95**, 523.
2 G. A. Somorjai, R. L. York, D. Butcher and J. Y. Park, *Phys. Chem. Chem. Phys.*, 2007, **9**, 3500.
3 H. Oosterbeek, *Phys. Chem. Chem. Phys.*, 2007, **9**, 3570.
4 J. Assmann, V. Narkhede, N. A. Breuer, M. Muhler, A. P. Seitsonen, M. Knapp, D. Crihan, A. Farkas, G. Mellau and H. Over, *J. Phys.: Condens. Matter*, 2008, **20**, 184017.
5 C. R. Henry, *Surf. Sci. Rep.*, 1999, **31**, 231.
6 H. J. Freund, H. Kuhlenbeck, J. Libuda, G. Rupprechter, M. Bäumer and H. Hamann, *Top. Catal.*, 2001, **15**, 201.
7 S. Haq and R. Raval, *Phys. Chem. Chem. Phys.*, 2007, **9**, 3641.
8 S. Dahl, P. A. Taylor, E. Törnqvist and I. Chorkendorff, *J. Catal.*, 1998, **178**, 679.

9 S. Dahl, A. Logadottir, R. C. Egeberg, J. H. Larsen, I. Chorkendorff, E. Törnqvist and J. K. Nørskov, *Phys. Rev. Lett.*, 1999, **83**, 1814.

10 R. A. Dalla'Betta and M. Shelef, *J. Catal.*, 1977, **48**, 111.

11 H. Abrevaya, M. J. Cohn, W. M. Targos and H. J. Robota, *Catal. Lett.*, 1990, **7**, 183.

12 R. J. Madon, S. C. Reyes and E. Iglesia, *J. Phys. Chem.*, 1991, **95**, 7795.

13 E. Shincho, C. Egawa, S. Naito and K. Tamaru, *Surf. Sci.*, 1985, **149**, 1.

14 J. C. Fuggle, E. Umbach, P. Feulner and D. Menzel, *Surf. Sci.*, 1977, **64**, 69.

15 H. Pfnür, P. Feulner, H. A. Engelhardt and D. Menzel, *Chem. Phys. Lett.*, 1978, **59**, 481.

16 P. Feulner, H. A. Engelhardt and D. Menzel, *Appl. Phys.*, 1978, **15**, 355.

17 J. A. Schwarz and S. R. Kelemen, *Surf. Sci.*, 1979, **87**, 510.

18 H. Pfnür, P. Feulner and D. Menzel, *J. Chem. Phys.*, 1983, **79**, 4613.

19 T. Yamada, Y. Iwasawa and K. Tamaru, *Surf. Sci.*, 1989, **223**, 527.

20 E. D. Westre, D. E. Brown, J. Kutzner and S. M. George, *Surf. Sci.*, 1994, **302**, 280.

21 T. Zubkov, G. A. Morgan and J. T. Yates, *Chem. Phys. Lett.*, 2002, **362**, 181.

22 T. Zubkov, G. A. Morgan, J. T. Yates, O. Kühlert, M. Lisowski, R. Schillinger, D. Fick and H. J. Jänsch, *Surf. Sci.*, 2003, **526**, 57.

23 T. E. Madey, *Surf. Sci.*, 1979, **79**, 575.

24 G. E. Thomas and W. H. Weinberg, *J. Chem. Phys.*, 1979, **70**, 1437.

25 H. Pfnür, D. Menzel, F. M. Hoffmann, A. Ortega and A. M. Bradshaw, *Surf. Sci.*, 1980, **93**, 431.

26 E. D. Williams and W. H. Weinberg, *Surf. Sci.*, 1979, **82**, 93.

27 G. Michalk, W. Moritz, H. Pfnür and D. Menzel, *Surf. Sci.*, 1983, **129**, 92.

28 H. Pfnür and D. Menzel, *Surf. Sci.*, 1984, **148**, 411.

29 P. Jakob, *J. Chem. Phys.*, 2004, **120**, 9286.

30 S. Kneitz, J. Gemeinhardt and H. P. Steinrück, *Surf. Sci.*, 1999, **440**, 307.

31 S. H. Payne, J. S. McEwen, H. J. Kreuzer and D. Menzel, *Surf. Sci.*, 2005, **594**, 240.

32 S. B. Vendelbo, M. Johansson, D. J. Mowbray, M. P. Andersson, F. Abild-Pedersen, J. H. Nielsen, J. K. Nørskov and I. Chorkendorff, *Top. Catal.*, 2010, **53**, 357.

33 P. D. Reed, C. M. Comrie and R. M. Lambert, *Surf. Sci.*, 1976, **59**, 33.

34 R. Ku, N. A. Gjostein and H. P. Bonzel, *Surf. Sci.*, 1977, **64**, 465.

35 G. Lauth, T. Solomun, W. Hirschwald and K. Christmann, *Surf. Sci.*, 1989, **210**, 201.

36 G. Rotaris, A. Baraldi, G. Comelli, M. Kiskinova and R. Rosei, *Surf. Sci.*, 1996, **359**, 1.

37 J. Wang, Y. Wang and K. Jacobi, *Surf. Sci.*, 2001, **488**, 83.

38 J. G. McCarty and H. Wise, *Chem. Phys. Lett.*, 1979, **61**, 323.

39 G. G. Low and A. T. Bell, *J. Catal.*, 1979, **57**, 397.

40 E. Zağli and J. L. Falconer, *J. Catal.*, 1981, **69**, 1.

41 H. M. Miura, M. L. McLaughlin and R. D. Gonzalez, *J. Catal.*, 1983, **79**, 227.

42 N. Kakuta and J. M. White, *J. Catal.*, 1986, **97**, 150.

43 R. M. Nielsen, S. Murphy, C. Strebel, M. Johansson, J. H. Nielsen and I. Chorkendorff, *Surf. Sci.*, 2009, **603**, 3420.

44 R. M. Nielsen, S. Murphy, C. Strebel, M. Johansson, I. Chorkendorff and J. H. Nielsen, *J. Nanopart. Res.*, 2010, **12**, 1249.

45 J. H. Nielsen, L. Bech, K. Nielsen, Y. Tison, K. P. Jørgensen, J. L. Bonde, S. Horch, T. F. Jaramillo and I. Chorkendorff, *Surf. Sci.*, 2009, **603**, 1182.

46 F. Besenbacher, E. Lægsgaard, K. Mortensen, U. Nielsen and I. Stensgaard, *Rev. Sci. Instrum.*, 1988, **59**, 1035.

47 S. Murphy, R. M. Nielsen, M. Johansson and J. H. Nielsen, *Carbon*, 2011, **49**, 376.

48 Therefore, some surface defects may have been formed on the HOPG by accelerated positive Ru ions coming from the electron-beam evaporator.

49 Our measurements indicated a concentration of approximately 1% $^{13}C^{18}O$ in the $^{13}C^{16}O$ dosing gas.

50 The only differences were that the reduction step was carried out for 20 min and the final anneal step in UHV was carried out at 1400 K for 2 min.

51 The corresponding diameter of a sphere with the selected mass is used to identify the nanoparticles.

52 C. Park, W. G. Durrer, H. Poppa and J. T. Dickinson, *J. Catal.*, 1985, **95**, 361.

53 P. A. Redhead, *Vacuum*, 1962, **12**, 203.

54 I. Chorkendorff and J. W. Niemantsverdriet, *Concepts of Modern Catalysis and Kinetics*, Wiley, 2007.

55 J. Gavnholt and J. Schiøtz, *Phys. Rev. B: Condens. Matter*, 2008, **77**, 035404.

56 Here we have used the notation for stepped surfaces to describe the Ru(1 1 10) surface.

57 P. Jakob, M. Gsell and D. Menzel, *J. Chem. Phys.*, 2001, **114**, 10075.

58 G. L. Bezemer, J. H. Bitter, H. P. C. E. Kuipers, H. Oosterbeek, J. E. Holewijn, X. Xu, F. Kapteijn, A. J. van Dillen and K. P. de Jong, *J. Am. Chem. Soc.*, 2006, **128**, 3956.

59 H. I. Lee, B. E. Koel, W. M. Daniel and J. M. White, *J. Catal.*, 1982, **74**, 192.

60 K. L. Kostov, H. Rauscher and D. Menzel, *Surf. Sci.*, 1992, **278**, 62.

61 M. Mavrikakis, B. Hammer and J. K. Nørskov, *Phys. Rev. Lett.*, 1998, **81**, 2819.

62 N. Tian, Z. Y. Zhou, S. G. Sun, Y. Ding and Z. L. Wang, *Science*, 2007, **316**, 732.